JOURNAL OF AIRCRAFT
Vol. 39, No. 5, September–October 2002

Unsteady Separation Processes and Leading Edge Vortex Precursors: Pitch Rate and Reynolds Number Influences

Scott J. Schreck*
National Wind Technology Center, Golden, Colorado 80401
William E. Faller†
Applied Simulation Technologies, Cape Canaveral, Florida 32920-0883
and
Michael C. Robinson‡
National Wind Technology Center, Golden, Colorado 80401

A NACA 0015 airfoil was pitched at constant rate through static stall to elevated angles of attack. Time-dependent shear stress measurements were performed near the airfoil leading edge. Using these data, unsteady boundary layer processes preceding leading edge vortex emergence were characterized for a broad range of nondimensional pitch rate and Reynolds number. In addition, steady data were acquired and examined to furnish a baseline for analysis and comparison. Overall, the analyses revealed a progression of events culminating in leading edge vortex emergence. Analyses allowed the independent influences of nondimensional pitch rate and Reynolds number upon this progression to be ascertained and inferences to be drawn regarding the structure of the resulting local flowfield.

Nomenclature

c	=	airfoil chord, m
Re_c	=	chord Reynolds number
s	=	distance from leading edge along airfoil surface, cm
t	=	time, s
t_{nd}	=	nondimensional time, tU_∞/c
U_∞	=	test section velocity, m/s
x	=	distance from leading edge along airfoil chordline, cm
α	=	instantaneous angle of attack, deg
α^+	=	nondimensional pitch rate, $c\dot{\alpha}/U_\infty$
$\dot{\alpha}$	=	pitch rate, rad/s

Introduction

POTENTIAL performance enhancements to wind energy machines, rotorcraft, and fixed wing aircraft continue to prompt intense study of unsteady separated flowfields. When a lifting surface pitches through static stall to elevated angles of attack, the unsteady boundary layer separates and gives rise to an energetic leading edge vortex. This vortex grows as it convects downstream over the lifting surface and finally sheds into the wake. Associated with vortex development and demise are accompanied by brief but substantial lift augmentation catastrophic stall.

Much effort has been directed toward characterizing and understanding unsteady separated flows.[1] However, only limited success has been attained in predicting and mitigating the adverse effects of unsteady flowfields dominated by large energetic vortices. Clarified comprehension of leading edge vortex initiation and improved modeling would accelerate progress toward controlling unsteady flowfields and mitigating the associated adverse effects.[2]

Presented as Paper 2000-2605 at the AIAA Fluids 2000 Conference, Denver, CO, 19–21 June 2000; received 26 March 2001; revision received 9 September 2001; accepted for publication 8 January 2002.

*National Renewable Energy Laboratory, 1617 Cole Blvd; scott_schreck@nrel.gov.
†P.O. Box 883.
‡National Renewable Energy Laboratory, 1617 Cole Blvd.

Previous experimental investigations have identified significant aspects of unsteady boundary layer separation, especially unsteady boundary layer reversal. Carr et al.[3] experimentally isolated three distinct types of unsteady boundary layer reversal on a pitching airfoil, all of which led to classical dynamic stall. Koromilas and Telionis[4] found that a very thin layer of reversed flow precedes a more violent region, wherein substantial disturbances are likely to take place. Schreck and Luttges[5] observed that reverse flows originating near the trailing edge of a pitching airfoil were incidental to unsteady vortex initiation near the leading edge. Using unsteady shear stress measurements, Schreck et al.[6,7] documented the combined influences of α^+ and Re_c on unsteady boundary processes over a limited parameter range. Subsequent experiments using constant rate[8,9] and sinusoidal[10] pitching linked specific features in shear stress records with pertinent structures and processes in the unsteady boundary layer.

Several computational efforts also have affirmed the role of unsteady boundary layer reversal. Visbal[11] showed that, at low Re_c, the leading edge vortex on a pitching airfoil is initiated by the roll up of a strong shear layer created by a thin unsteady region of flow reversal. Gendrich et al.[12] confirmed the role of unsteady boundary layer reversal in vortex initiation, and further noted that these reversals were confined to the airfoil leading edge region at elevated α^+. Ghia et al.[13] linked size and strength of the leading edge separation bubble to vortex strength and formation time. Knight and Choudhuri[14] computed the topology of unsteady boundary layer reversal on a pitching airfoil and correlated the appearance of critical points in the topology to reverse flow regions and leading edge vortex emergence. Reisenthel[15] concluded that unsteady flows over airfoils remained self-similar throughout an extended Re_c range and identified a topological center within the lifting vorticity layer as the source of vortex formation.

Unsteady boundary layer transition and the role it plays in unsteady separated flowfield development have been examined, as well. The prominent influence of transition on unsteady flowfields has been affirmed by Ericsson[16] for both attached and separated unsteady flows. Lorber and Carta[17] have experimentally characterized unsteady boundary layer transition and relaminarization on a pitching wing. Wilder et al.[18] have experimentally demonstrated that the dynamic stall process is quite sensitive to the boundary layer turbulence state. Carr and Cebeci[19] have shown numerically that dynamic stall greatly alters transition location on a pitching airfoil.

However, no investigation has been carried out to ascertain the independent influences of Re_c and α^+ on unsteady boundary layer processes through a parameter range extending from high α^+, through quasi-steady conditions, and reaching steady state. The current work employs time-dependent shear stress measurements to characterize unsteady boundary layer processes culminating in leading edge vortex inception on a pitching airfoil over an extended α^+ range. Using this information, physical mechanisms responsible for these events were postulated.

Experimental Methods

Unsteady shear stress measurements were performed in the Frank J. Seiler 0.91 m × 0.91 m wind tunnel located at the U.S. Air Force Academy. The model was an aluminum NACA 0015 airfoil, with chord and span lengths of 15.24 and 76.84 cm. Each end of the airfoil was capped with a circular splitter plate that was 0.32 cm thick, 30.48 cm in diameter, and machined to a sharp edge around the perimeter. The airfoil model was mounted vertically in the test section center, with the upper and lower ends of the model connected to steel shafts mounted in ball bearings. Airfoil pitching was driven at the lower shaft by a 3.5 hp stepper motor through a 4:1 gear linkage. Airfoil pitch axis was located at 0.25c throughout these experiments.

A thin film, multiple element array of shear stress sensors was applied to the airfoil surface, placing the sensor row parallel to the chord line and 40.64 cm below the upper splitter plate. The array was wrapped around the entire airfoil contour, and the array edges were placed at the trailing edge. This prevented the array from introducing surface irregularities in the leading edge region. Individual nickel sensor elements on the array were 1.65 mm long (spanwise), 0.13 mm wide (chordwise), and 0.3 μm thick. Nominal sensor cold resistance was 6.0 Ω. The entire array contained a total of 124 sensors spaced 2.54 mm apart. Construction and use of these thin film arrays previously have been described in detail.[20,21]

The 15 upper surface sensors nearest the leading edge were connected to constant temperature hot wire anemometers. Figure 1 shows the leading 0.25c and the locations of the 15 sensors on the airfoil section with sensor 1 at the leading edge. Anemometer overheat resistance ratios were set at 1.10. Separate experiments determined that sensor heat fluxes at this overheat were low enough to avoid tripping either the steady or unsteady boundary layers examined in the current investigation. Anemometer bandwidths were set at 10 kHz using the square wave test.

To increase the dynamic range of the data, anemometer signals were routed through bias subtraction modules prior to amplification and discretization. The bias subtraction modules maximized signal-to-noise ratio and reliability by minimizing active circuit components. This was achieved at the minor expense of inverted output signal. Tests confirmed flat frequency response beyond 10 kHz. After bias subtraction, signals were low-pass filtered (1 and 10 kHz cutoff) and amplified by gains of 20–100. Gain was dictated by signal magnitudes and analog-to-digital converter input range. Signals were then sampled and digitized at 2 kHz (for 1 kHz cutoff) and 20 kHz (for 10 kHz cutoff) by a 12-bit analog-to-digital converter.

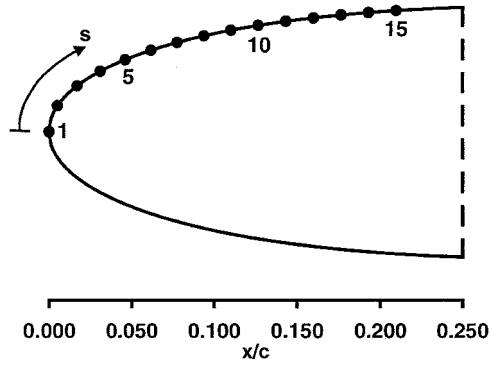

Fig. 1 NACA 0015 leading edge region cross section showing shear stress sensor locations.

Table 1 Experimental parameter range

Test section velocity, m/s	Pitch rate, deg/s			
	92.0	183.0	367.0	733.0
3.1	——	0.16	0.32	0.64
6.1	0.04	0.08	0.16	0.32
12.2	——	0.04	0.08	0.16
24.4	0.01	0.02	0.04	0.08

The current work included $U_\infty = 3.1, 6.1, 12.2$, and 24.4 m/s, corresponding to $Re_c = 2.4 \times 10^4, 4.8 \times 10^4, 9.6 \times 10^4$, and 1.92×10^5. All dynamic experiments employed constant rate pitching that began at $\alpha = 0.0$ deg and ended at $\alpha = 60.0$ deg, at 92, 183, 367, and 733 deg per second. Pitching motions were highly linear and largely free from acceleration or deceleration transients.[22,23] Further, the events analyzed in the current work occurred in the intermediate α range, where transients were undetectable.

These parameter combinations yielded the α^+ values in Table 1. Data were acquired and analyzed at these 14 combinations of α^+ and Re_c, allowing the independent effects of α^+ and Re_c to be ascertained. For each parameter combination α and the 15 shear stress signals were sampled at 2 kHz during 20 consecutive airfoil pitch repetitions and ensemble averaged. Ensemble averaging, in conjunction with inherently high signal-to-noise ratio, ensured that signal features identified for characterization and analysis represented pertinent fluid dynamic events instead of extraneous noise. In addition, for all α^+ values except 0.01 and 0.02, α and the 15 shear stress signals were sampled at 20 kHz during a single pitch.

Static α measurements also were performed at all four Re_c values. Starting at $\alpha = 0.0$ deg, α was incremented in 0.9 deg steps to a maximum of 22.5 deg. After each 0.9 deg step, 1.0 s was allowed to elapse to stabilize the flowfield. Then, 100 samples were acquired at a 2 kHz sample rate. This process was repeated twice at each Re_c, yielding two data sets to assess repeatability.

Prior to acquiring the data employed in the current study, systematic validation tests were carried out. Initial tests at a fixed airfoil α and constant U_∞ demonstrated that the system just described remained stable during extended periods of operation. Further, ambient temperature was well controlled, and fluctuations were negligible.

As just stated, the bias subtraction modules inverted the anemometer output signal. As such, straightforward procedures were employed to clearly establish the relationship between shear stress variations and recorded signal level excursions. With the airfoil held at $\alpha = 0.0$ deg, the anemometer output signal was recorded during slow variations in U_∞. This confirmed that, for the system configured as described earlier, decreasing shear stress prompted increasing anemometer output signal levels and vice versa.

Results and Discussion

Steady Boundary Layer Data and Analysis

Steady boundary layer characterizations were undertaken in the current study for two purposes. First, the well understood steady boundary layer provided an environment for developing physically pertinent interpretations of unfamiliar and complex dynamic shear stress records. Second, steady boundary layer kinematics furnished a reference baseline that allowed isolation of unsteady boundary layer structures and processes.

The shear stress sensors reliably detected steady boundary layer separation and transition. Sensors near the separation point showed definite pseudo-sinusoidal shear stress fluctuations with time. With the separation point between two adjacent sensors, shear stress fluctuations at these two sensors exhibited a clear 180 deg phase relationship. Boundary layer transition caused a marked increase in shear stress mean and standard deviation. This performance is consistent with that documented by Stack et al.[20] and Mangalam et al.[21] in validation tests of this technique.

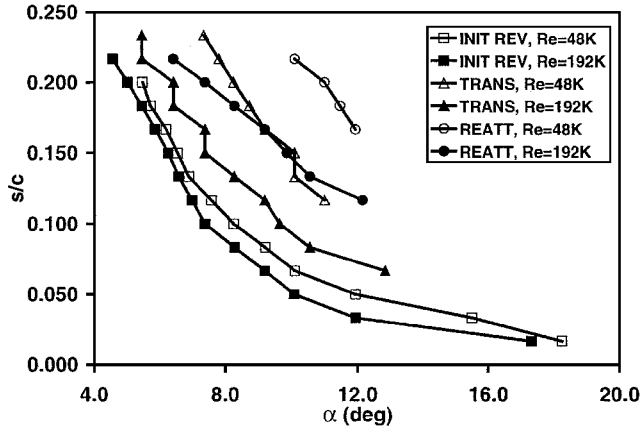

Fig. 2 Static laminar separation, incipient transition, and reattachment movement with α.

To characterize steady boundary layer kinematics, the airfoil was incremented through 25 static angles of attack. At low α this procedure revealed unambiguous 180 deg phase relationships between adjacent traces, indicating laminar boundary layer separation. Further α increases caused shear stress mean and standard deviation to begin rising gradually, indicating incipient transition. Soon these incipient rises were supplanted by abrupt growth in shear stress mean and standard deviation, signaling peak boundary layer transition. This occurred at higher α for sensors nearer the leading edge, indicating forward progress with higher α. Following transition, 180 deg phase relationships between spatially adjacent traces were again evident, caused by laminar separation bubble closure via turbulent shear layer reattachment.[20,21]

Representative steady boundary layer separation, transition, and reattachment progressions are shown in Fig. 2, for $Re_c = 4.8 \times 10^4$ and 1.92×10^5. In Fig. 2 laminar separation movement with α is shown by the lower set of curves, marked with square symbols. For both Re_c values separation was observed initially near sensor 15 and moved forward on the airfoil with increasing α. Higher Re_c prompted separation to occur at lower α. Transition consistently remained downstream of separation and thus did not influence this event.

Figure 2 also displays incipient boundary layer transition, shown by the curves marked with triangular symbols. Incipient boundary layer transition occurred downstream of separation, being first observed at sensor 15 and progressing forward with increasing α. Higher Re_c reduced the distance between separation and incipient transition as a result of elevated boundary layer receptivity to disturbance and propensity to undergo transition.

Boundary layer reattachment also is documented in Fig. 2, defining the downstream boundary of the separation bubble. Reattachment was first observed at sensor 15 and progressed forward with increasing α. The distance between separation and reattachment shortened at higher Re_c as a result of earlier transition. Static peak boundary layer transition (not shown herein) was well correlated with reattachment, consistent with previous work.[20,21] Laminar separation bubble data herein agree well with previous measurements[24] in the same Re_c range.

Unsteady Boundary Layer Data and Analysis

Unsteady shear stress data acquired in this experiment were detailed and complex and were a challenge to analyze and interpret in a physically pertinent manner. However, static data were found to be valuable as a datum for isolating dynamic increments and as a guide for identifying specific shear stress features. Additional clarification was obtained using prior research carried out in the dynamic regime.[6,7]

Figure 3 contains ensemble averaged anemometer output signals acquired during 20 consecutive airfoil pitch motions for $\alpha^+ = 0.08$ and $Re_c = 9.6 \times 10^4$. Sensor locations are identified by the numbers near the left end of each trace. Higher anemometer output signals indicate lower shear stress, and absolute references have been omitted.

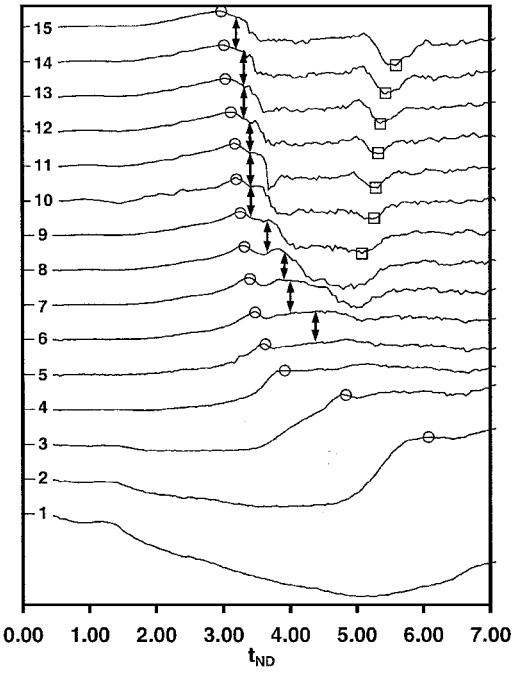

Fig. 3 Typical dynamic shear stress mean histories: $Re_c = 9.6 \times 10^4$ and $\alpha^+ = 0.08$.

As airfoil pitching began at $t_{nd} = 0.0$, shear stress decreased gradually at sensors 4 through 15, culminating in definite shear stress minima marked by circular symbols. At sensors 2 and 3 shear stress first increased before decreasing and attaining minima, also marked by circular symbols. At sensor 1 shear stress first increased and then decreased, but reached no local minimum. Examination of adjacent traces revealed that 180 deg phase relationships occurred in conjunction with these shear stress minima. Simultaneous presence of minimum shear stress levels and 180 deg phase relationships indicated reverse flow near the airfoil surface. Prior work has established that a thin reverse flow layer precedes more expansive unsteady separation events, but precise experimental detection of unsteady separation itself remains ambiguous.[4]

In Fig. 3, after attaining minima, shear stress began to increase at sensors 3 through 15. As unsteady shear stress increased, 180 deg phase relationships occurred between adjacent signals, but were not associated with shear stress extrema. These 180 deg phase relationships began at the times indicated by the vertical double-ended arrows. After initial occurrence these 180 deg phase relationships persisted for a time period not readily quantifiable because of the ambiguity of cessation. Shortly thereafter, shear stress at sensors 8 through 15 increased sharply and remained at elevated levels for approximately 1.0–2.0t_{nd} units. After this, shear stress at sensors 9 through 15 reached clear maxima, marked in Fig. 3 by square symbols. Correlation with unsteady surface pressure data[6] linked these shear stress maxima with leading edge vortex initiation and passage.

In addition to mean shear stress levels, standard deviations also were computed for the ensemble of 20 successive pitch motions. Figure 4 contains a typical plot of shear stress standard deviation for $\alpha^+ = 0.08$ and $Re_c = 9.6 \times 10^4$. Airfoil pitching began at $t_{nd} = 0.0$, and sensor locations correspond to the numbers on the traces. In Fig. 4 no sensors show any significant standard deviation rise until well after airfoil pitching begins. Incipient standard deviation rise (circular symbols) is observed first at sensor 15 at $t_{nd} = 3.15$ and then at sensors nearer the leading edge at later times. Following incipient rise, standard deviation levels increase steadily at sensors 4 through 15, soon reaching clear maxima (square symbols). After reaching peak levels, standard deviations decrease perceptibly, but do not decline to levels present prior to incipient standard deviation rise.

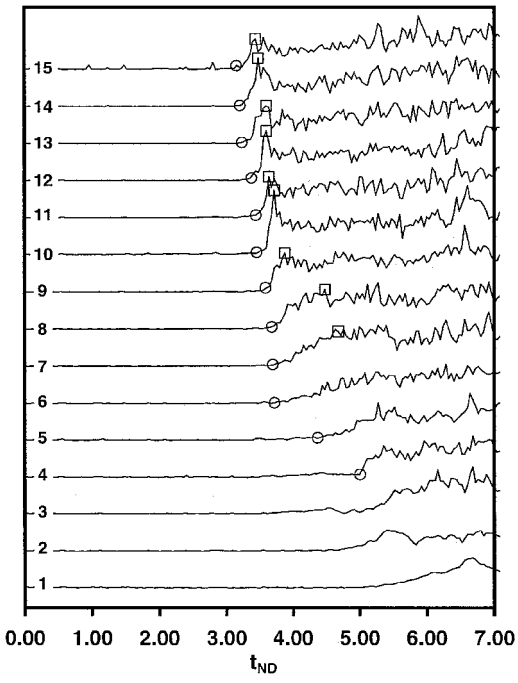

Fig. 4 Typical dynamic shear stress standard deviation histories. $Re_c = 9.6 \times 10^4$ and $\alpha^+ = 0.08$.

The four processes just introduced (boundary layer reversal, initial phase reversal, standard deviation incipient rise, and standard deviation peak) were characterized at static conditions and at seven values of α^+ encompassing four levels of Re_c. Pitch rate constraints prevented the full α^+ range from being achieved at a single Re_c. However, this detracted little from the analyses herein, as Re_c exercised a secondary influence on unsteady boundary layer processes.

Subsequent plots documenting boundary layer reversal, initial phase reversal, standard deviation incipient rise, and standard deviation peak employ α on the abscissa. For these plots uncertainty in α increased with airfoil pitch rate, reaching a maximum of ± 0.18 deg at the highest pitch rate of 733 deg per second.

Unsteady Boundary Layer Reversal

Unsteady boundary layer reversal, as described in conjunction with Fig. 3, was observed for all 14 combinations of α^+ and Re_c. For each of the 14, the set of α when reversal first occurred at each s/c was recorded and plotted. A representative set of boundary layer reversal trajectories, for the experimental range of α^+ and including static data, appears in Fig. 5. In Fig. 5 steady separation (identified as STA) was first observed at sensor 14. Thereafter, it advanced forward at constant rate with increasing α until $s/c = 0.100$, where it progressively decelerated as separation continued to advance, being last observed at $s/c = 0.017$.

Forward movement of unsteady boundary layer reversal, for $\alpha^+ = 0.01$ through 0.08, was similar to that observed under static conditions. Unsteady boundary layer reversal was first observed at sensor 15 and propagated forward to $s/c = 0.100$ at approximately constant rate. Subsequently, boundary layer reversal continued to move forward toward the leading edge, but slowed as it moved. The main effect of increasing α^+ in this range was the delay of unsteady boundary layer reversal to higher α. These trends have been observed in other experiments.[8,9]

At $\alpha^+ = 0.16$ unsteady boundary layer reversal was first observed at sensor 15, but no longer moved forward at constant rate. Instead, unsteady boundary layer reversal began moving forward from sensor 15 at high speed, but soon began to decelerate, continuing to do so until reaching $s/c = 0.167$. Here, forward movement suddenly accelerated, and continued at high speed until passing $s/c = 0.100$, where deceleration began once again.

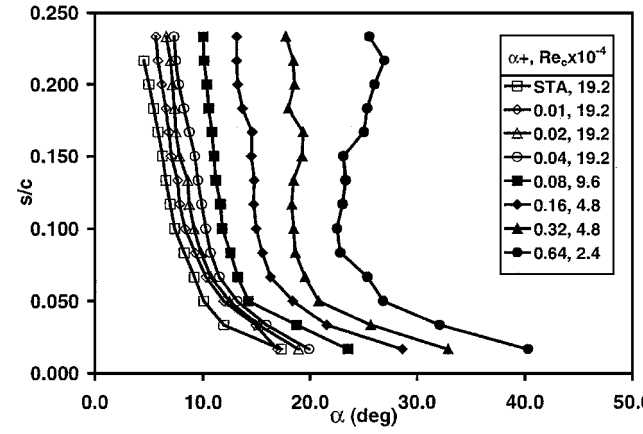

Fig. 5 Boundary layer reversal movement with α for experimental range of α^+.

At $\alpha^+ = 0.32$ and 0.64 a fundamentally different trend in boundary layer reversal movement was apparent. In this range boundary layer reversal was first observed ahead of sensor 15, propagating concurrently forward and aft with increasing α. At $\alpha^+ = 0.64$ unsteady boundary layer reversal was first seen at $s/c = 0.100$, and at $\alpha^+ = 0.32$ initial reversal occurred simultaneously at $s/c = 0.183$ and 0.117. From these initial points boundary layer reversal simultaneously advanced both forward and aft. As at lower values of α^+, boundary layer reversal for $0.16 \leq \alpha^+ \leq 0.64$ also was delayed to higher α by increasing α^+.

The foregoing data demonstrate that, for all Re_c levels, unsteady boundary layer reversal changed substantially with α^+. Increasing α^+ consistently delayed this event to higher α. At sufficiently elevated α^+, reversal was fundamentally altered, first occurring forward of sensor 15 and then simultaneously moving forward and aft. In all cases unsteady boundary layer reversal involved fleeting shear stress minima and phase reversals, analogous to static separation.

Greater leading edge localization of unsteady boundary layer reversal with higher α^+ is consistent with prior experiments,[5,6,7] computations,[12] and vorticity models.[25] Higher α^+ also delayed unsteady boundary layer reversal to higher α, consistent with delays imposed by diffusion timescales.[22] That unsteady boundary layer reversal trajectories at low α^+ strongly resemble those for static separation suggests that these two events are highly similar at low α^+.

Initial Phase Reversal

As described in conjunction with Fig. 3, phase reversals not associated with shear stress extrema occurred for all 14 combinations of α^+ and Re_c. These phase reversals consistently followed boundary layer reversal, and the two events remained clearly distinct. Surface locations and α corresponding to initial phase reversal occurrence were recorded and plotted for the experimental range of α^+ and Re_c. Phase reversal persisted for a finite time after initial occurrence, but phase reversal cessation was difficult to reliably detect. Thus, phase reversal duration was thus not quantified herein. Figure 6 shows a typical set of initial phase reversal trajectories for the experimental α^+ range and for static conditions.

In Fig. 6 static phase reversal (identified as STA), corresponding to boundary layer reattachment, is first observed at sensor 14, proceeds forward, and is last seen at $s/c = 0.117$ at $\alpha = 12.2$ deg. In the range $0.01 \leq \alpha^+ \leq 0.04$ initial phase reversal is first observed at $s/c = 0.200$ and advances forward from there to $s/c = 0.067$. Notably, the three curves for $\alpha^+ = 0.01$, 0.02, and 0.04 cross the static curve because of the slower rate of advance under static conditions.

The curve for $\alpha^+ = 0.08$ was slightly different from the first three, as it broke sharply at $s/c = 0.133$, indicating abrupt deceleration. At $\alpha^+ = 0.16$ phase reversal movement changed dramatically. Here, it was initially observed at $s/c = 0.200$, instead of at sensor 15, and then simultaneously moved both upstream and downstream with increasing α. Similar trends were apparent for $\alpha^+ = 0.32$ and 0.64. At these α^+ values phase reversal was first observed at 0.117 and

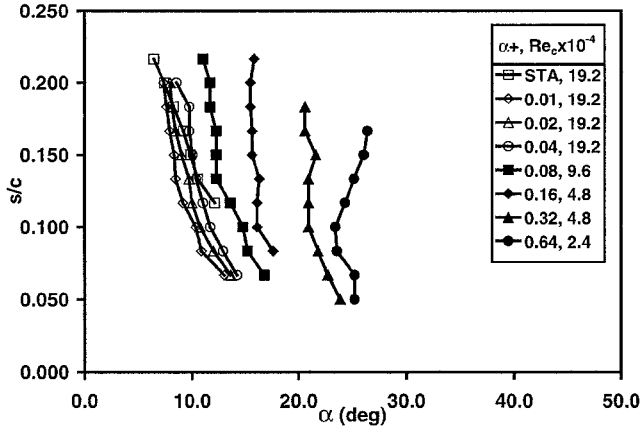

Fig. 6 Initial phase reversal movement with α for experimental range of α^+.

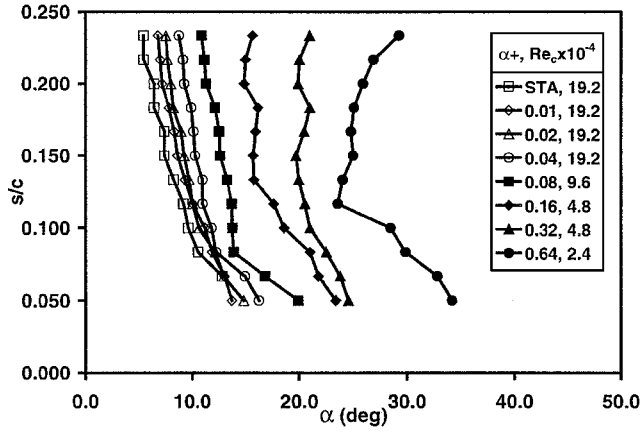

Fig. 7 Incipient standard deviation rise movement with α for experimental range of α^+.

0.100, respectively, concurrently moving both forward and aft with increasing α. As with dynamic boundary layer reversal, higher α^+ levels delayed initial phase reversal to higher α.

Generally, the trends in initial phase reversal resembled those for boundary layer reversal. At static conditions and low α^+ both were first observed near sensor 15 and advanced forward with airfoil pitching. At elevated α^+ both occurred first at intermediate sensor locations and then simultaneously moved forward and aft with increasing α. Greater α^+ delayed both to substantially higher α. At all times boundary layer reversal and initial phase reversal remained clearly distinct, with boundary layer reversal always preceding phase reversal.

The correlation between boundary layer reversal and phase reversal suggests a relationship analogous to that seen for static conditions. Under static conditions the upstream phase reversal signals laminar separation, whereas downstream phase reversal corresponds to turbulent reattachment. A similar relationship can exist in the unsteady regime. However, although the trajectories for static separation and low α^+ boundary layer reversal were similar, those for static and low α^+ phase reversal were conspicuously different. This disparity implies that reattachment is mediated by different mechanisms under static and dynamic conditions.

Standard Deviation Incipient Rise

Shear stress standard deviation was virtually zero as airfoil pitching began and began to increase only at moderate α levels. The α at which shear stress standard deviation began to rise from zero, as introduced in Fig. 4, was recorded for each sensor across the experimental range of α^+ and Re_c. A typical set of standard deviation incipient rise trajectories, for the experimental α^+ range and static data (identified as STA), appears in Fig. 7. In Fig. 7, for static conditions, standard deviation incipient rise is first observed

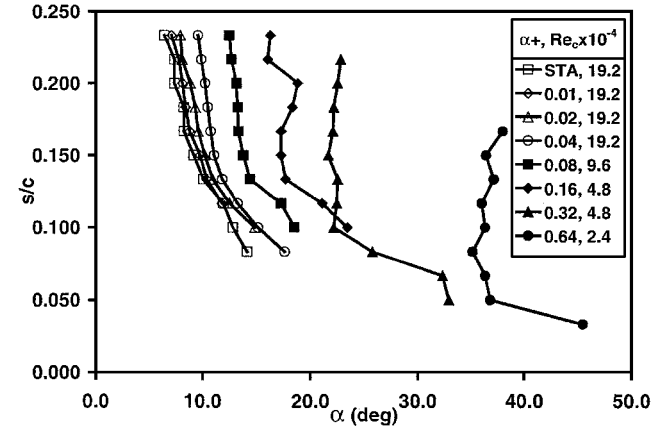

Fig. 8 Peak standard deviation movement with α for experimental range of α^+.

at sensor 15 and moves forward with increasing α until reaching $s/c = 0.067$.

For the dynamic range $0.01 \leq \alpha^+ \leq 0.08$, incipient rise first appears at sensor 15 and then proceeds forward with airfoil pitching to $s/c = 0.050$. At $\alpha^+ = 0.16$ and 0.32 standard deviation incipient rise curves are fundamentally different from those at lower α^+ values. At these elevated α^+ levels incipient rise first appears simultaneously at $s/c = 0.200$ and 0.150. From these points, incipient rise then simultaneously propagates both forward and aft as α increases. At $\alpha^+ = 0.64$ incipient rise occurs first at $s/c = 0.117$ and then moves forward and aft concurrently with airfoil pitching. Overall, greater α^+ delayed standard deviation incipient rise to higher α and confined this process more to the leading edge vicinity. Under static conditions standard deviation incipient rise represents incipient transition in the separated shear layer.[20,21]

Standard Deviation Peak

Following standard deviation incipient rise, shear stress standard deviation continued to increase and reached clear maxima at most sensors, as described in conjunction with Fig. 4. For these sensors α at which shear stress standard deviation peaked was recorded across the experimental range of α^+ and Re_c. Typical standard deviation peak trajectories, for the experimental range of α^+ and static data (identified as STA), appear in Fig. 8.

In Fig. 8, at static conditions, peak standard deviation corresponded to peak transition and turbulent reattachment of the separated shear layer, closing the separation bubble. For static conditions peak standard deviation was observed first at sensor 15 and advanced forward to $s/c = 0.083$. For dynamic conditions in the range $0.01 \leq \alpha^+ \leq 0.08$, movement of peak standard deviation with increasing α was quite similar to that for static conditions, moving forward with airfoil pitching and halting near $s/c = 0.100$. The principal alteration caused by the onset of dynamic conditions and increased α^+ was delay of peak standard deviation to higher α.

As with the preceding three processes, the fundamental character of peak standard deviation movement changed at elevated α^+. At $\alpha^+ = 0.16$ peak standard deviation first occurred at $s/c = 0.217$ and shortly thereafter at 0.167, advancing both forward and aft with increasing α. At $\alpha^+ = 0.32$ initial peak standard deviation was simultaneously recorded at $s/c = 0.150$ and 0.100 and concurrently moved both forward and aft with increasing α. Finally, at $\alpha^+ = 0.64$, peak standard deviation was first observed at $s/c = 0.083$ and then progressed both upstream and downstream with increasing α. In addition to altering the character of peak standard deviation movement, higher α^+ also delayed it to higher α. Under static conditions peak standard deviation indicates peak transition and shear layer reattachment.[20,21]

Reynolds Number Dependence

As shown by Figs. 5–8, α^+ exercised a strong, orderly influence on unsteady boundary layer reversal and reattachment, as well as

standard deviation incipient rise and standard deviation peak. Re_c influences on these processes were less pronounced, but still clear and consistent. These Re_c dependencies are shown in Fig. 9, where boundary layer reversal, phase reversal, incipient standard deviation rise, and peak standard deviation are plotted for three values of Re_c for $\alpha^+ = 0.08$. In Fig. 9 the four groups of plots have been displaced arbitrarily in α to facilitate viewing. However, relative α positions between the three curves in each group have been preserved and can be quantified using the scale in the upper right corner of the plot.

To clearly disclose these Re_c dependencies and display them in a compact manner, all α values in each curve were averaged to yield a single α_{avg}. Figure 9 shows that curves for the same α^+ and process (boundary layer reversal, reattachment, standard deviation incipient rise, or standard deviation peak) were highly similar for all Re_c levels. Because the curves, and therefore the data distributions, were strongly similar, averages of these distributions can be compared in a physically significant manner.

Figure 10 contains a plot of α_{avg} vs α^+ for unsteady boundary layer reversal. At $\alpha^+ = 0.04$ unsteady boundary layer reversal occurs at the lowest α_{avg} for $Re_c = 1.92 \times 10^5$ and at higher α_{avg} for lower values of Re_c. This trend is repeated for $\alpha^+ = 0.08, 0.16$, and 0.32. That unsteady boundary layer reversal takes place earlier at higher Re_c values is consistent with trends observed in these experiments for static boundary layer separation and consistent with trends observed in the same Re_c range in other experiments.[9] This, in turn, suggests that related mechanisms are responsible for static and dynamic boundary layer reversal on a pitching airfoil.

Figure 11 contains a plot of α_{avg} vs α^+ for initial phase reversal. Generally, phase reversal occurred later for higher Re_c. This trend in phase reversal with respect to α is opposite that observed for steady boundary layer reattachment. This observation, coupled with the pronounced discrepancies between static reattachment progression and dynamic phase reversal progression, strongly suggests that static and dynamic boundary layer reattachment are driven by fundamentally different processes.

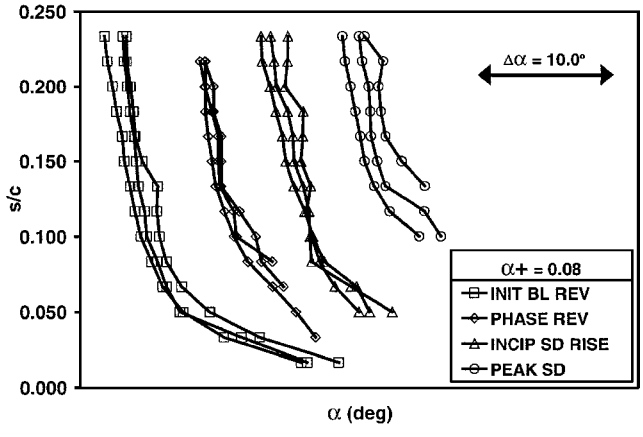

Fig. 9 Four unsteady boundary layer processes: $\alpha^+ = 0.08$ and $Re_c = 4.8 \times 10^4$, 9.6×10^4, and 1.92×10^5.

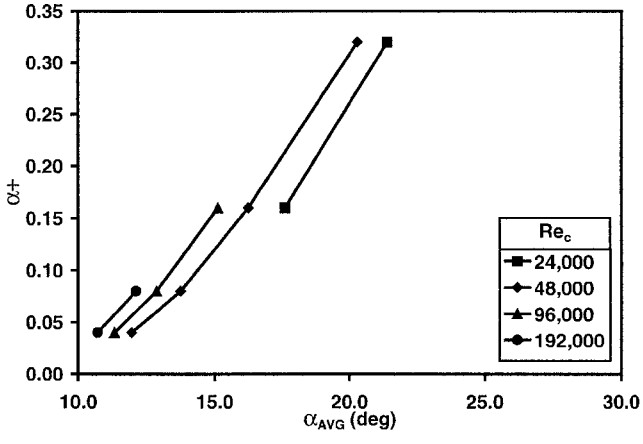

Fig. 10 Average α for boundary layer reversal.

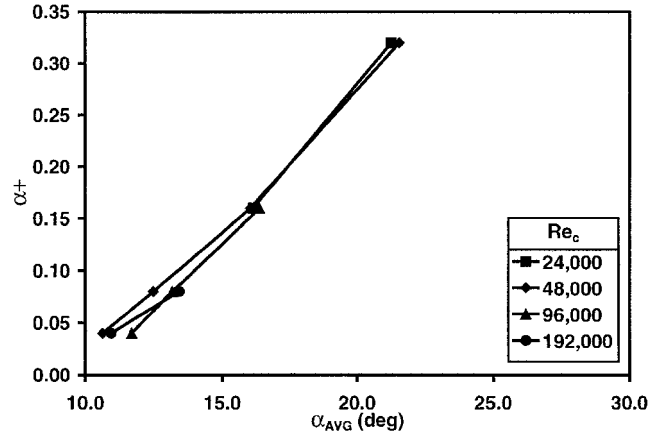

Fig. 11 Average α for initial phase reversal.

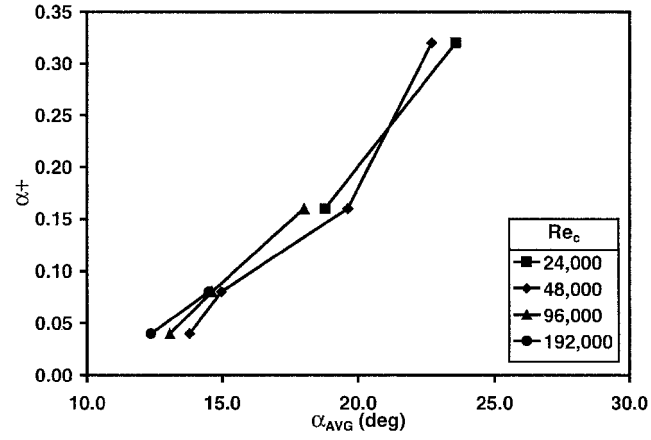

Fig. 12 Average α for incipient standard deviation rise.

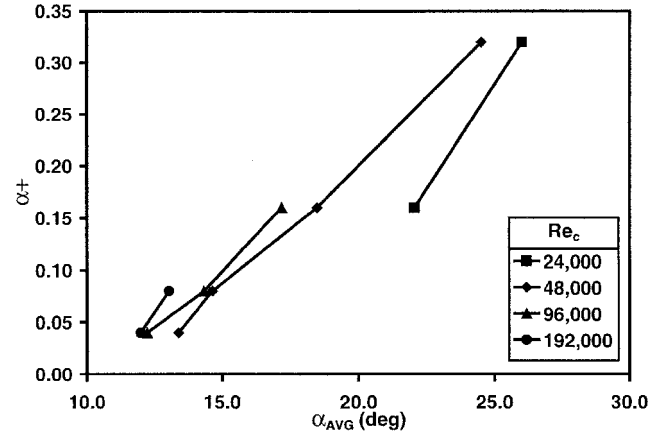

Fig. 13 Average α for peak standard deviation.

Figures 12 and 13 contain plots of α_{avg} vs α^+ for incipient standard deviation rise and peak standard deviation. In Figs. 12 and 13 higher Re_c levels drove incipient standard deviation rise and peak standard deviation to lower α_{avg}. However, peak standard deviation (Fig. 13) was somewhat more responsive to Re_c than incipient standard deviation rise (Fig. 12). Hence, the α_{avg} difference between these two processes exhibited a sensitivity to Re_c, as well. At $Re_c = 2.4 \times 10^4$ incipient rise and peak events were separated by approximately 3 deg in α_{avg}. This α_{avg} difference generally decreased as Re_c increased, implying dilation of the flow structures or processes separating these two.

Synthesis of Processes

Thus far, boundary layer reversal, phase reversal, incipient standard deviation rise, and peak standard deviation have been considered independently to allow thorough characterization. However, these processes must be analyzed collectively to understand the flow physics that give rise to the leading edge vortex.

Figure 14, corresponding to $\alpha^+ = 0.02$ and $Re_c = 1.92 \times 10^5$, places all four processes on one plot. Also included on the plot is initial leading edge vortex convection, determined as described with Fig. 3. Processes at this α^+ and Re_c are representative of those seen in the low α^+ range. Boundary layer reversal is the first event to be observed and is initially recorded by sensor 15 at $\alpha = 6.7$ deg. Boundary layer reversal then advances forward with airfoil pitching, reaching $s/c = 0.167$ when incipient standard deviation rise occurs at sensor 15 at $\alpha = 7.5$ deg. These two events then simultaneously propagate forward in response to increasing α. At $\alpha = 8.0$ deg phase reversal is detected at $s/c = 0.200$ and begins to move forward in close proximity to incipient standard deviation rise. Also at $\alpha = 8.0$ deg peak standard deviation is seen at sensor 15.

After $\alpha = 8.0$ deg all four processes were present on the airfoil, advancing forward as the airfoil continued to pitch up. As these four progressed forward, initial boundary layer reversal moved closer to both phase reversal and incipient standard deviation rise. At the same time the distance between these two events and peak standard deviation remained nearly constant. Finally, near $\alpha = 14$ deg phase reversal, incipient standard deviation rise, and peak standard deviation ceased to be observed. Shortly thereafter, the leading edge vortex began convecting from $s/c = 0.100$.

Figure 15, for $\alpha^+ = 0.32$ and $Re_c = 4.8 \times 10^4$, shows a progression for the four processes, which is typical for the high α^+ regime. Here, boundary layer reversal was detected nearly simultaneously

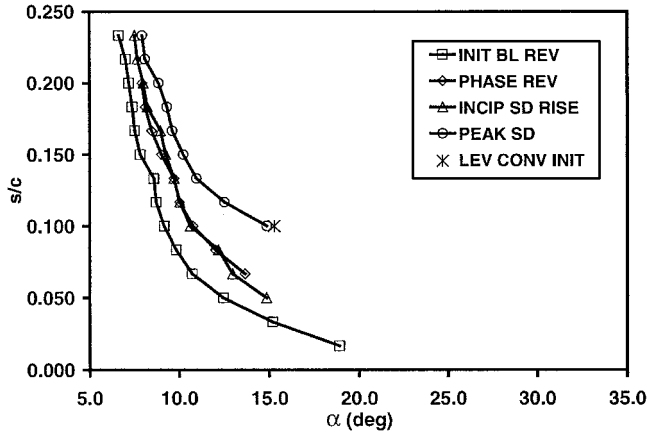

Fig. 14 Four unsteady boundary layer processes for $\alpha^+ = 0.02$ and $Re_c = 1.92 \times 10^5$.

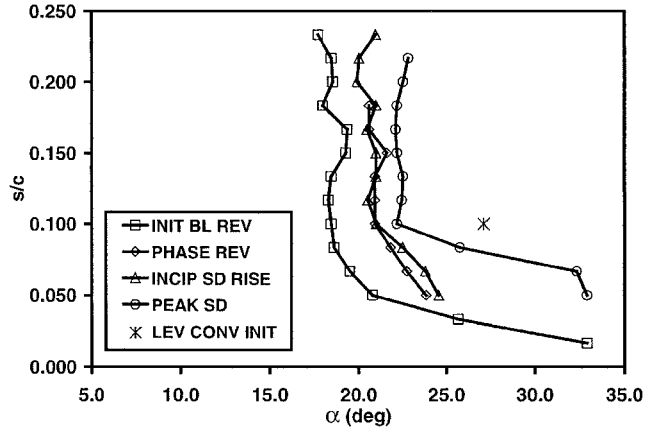

Fig. 15 Four unsteady boundary layer processes for $\alpha^+ = 0.32$ and $Re_c = 4.8 \times 10^4$.

at $s/c = 0.233$, 0.183, and 0.117, at $\alpha = 17.7$, 18.0, and 18.3 deg, respectively. From these points boundary layer reversal moved concurrently forward and aft, advancing only forward after $\alpha = 19.4$ deg. As at lower α^+ levels phase reversal and incipient standard deviation rise coincided closely. Incipient standard deviation rise was observed nearly simultaneously at $s/c = 0.200$, 0.167, and 0.117, at $\alpha = 19.9$, 20.5, and 20.6 deg, respectively, moving both forward and aft from these locations with increasing α. A short time later, when phase reversal and incipient standard deviation rise had advanced forward to $s/c = 0.083$, peak standard deviation was observed simultaneously at $s/c = 0.100$ and 0.167. Finally, at $\alpha = 27.1$ deg the leading edge vortex began to convect downstream from $s/c = 0.100$.

Over the experimental α^+ range boundary layer reversal consistently was the first event detected, followed by phase reversal and incipient standard deviation rise and finally peak standard deviation. At low α^+ boundary layer reversal was observed nearest the leading edge, with phase reversal and incipient standard deviation rise downstream of boundary layer reversal and peak standard deviation occurring aft of these three events. At elevated α^+ the relative spatial relationships of these four events were not easily characterized because each event could be present at two or more surface locations at any given time. Over the experimental parameter range, the numbers of boundary layer reversal, phase reversal, incipient standard deviation rise, and peak standard deviation events present were all equal for any set of conditions. This one-to-one correspondence implies a set of consistent physical relationships between these four events.

Movement of these four processes with α was strongly governed by α^+. At low and medium α^+ all four initially were seen in succession near the sensor array aft end and moved forward with α. Alternatively, at elevated α^+ the four events first occurred at one or more sites near the array center and then concurrently moved both downstream and upstream. As these events moved with airfoil pitching, the spatio-temporal order just described was preserved.

That a one-to-one correspondence existed between boundary layer reversal and both phase reversal and incipient standard deviation rise implies a topological consistency analogous to that under static conditions. As such, phase reversal and incipient standard deviation are likely to represent reattachment of the shear layer originating near boundary layer reversal.

The mechanism responsible for reattachment remains unclear, however. Movement of static reattachment with α differed significantly from initial phase reversal movement under dynamic conditions. The rise in standard deviation could be attributable to shear layer transition and associated time variations in velocity and shear stress.[6,7] Alternatively, irregular shedding of vorticity from the reattachment zone could cause the standard deviation rise.[26] At elevated α^+ existence of multiple simultaneous boundary layer reversals, phase reversals, and incipient standard deviation rise points is consistent with multiple discrete structures noted in prior work.[15]

Initial phase reversal and incipient standard deviation rise were observed in close proximity to each other, coinciding more closely for higher Re_c. This is consistent with shear layer thinning at higher Re_c, which would render reattachment more spatially compact. Because phase reversal persisted after initial occurrence and standard deviation levels increased after the incipient event, standard deviation increase to peak levels was accompanied by phase reversal.

Leading edge vortex convection began near locations experiencing peak standard deviation levels, consistent with the presence of substantial vorticity concentrations in combination with unsteady vorticity accumulation and shedding. Leading edge vortex convection began with the near simultaneous cessation of initial phase reversal, incipient standard deviation rise, and peak standard deviation. This is consistent with prior work,[27] wherein vortex convection began with the demise of key leading edge flow features.

Conclusions

A two-dimensional NACA 0015 airfoil was pitched at constant rate through static stall to elevated α. Nonintrusive unsteady

shear stress measurements of high spatial and temporal resolution were acquired near the leading edge. Unsteady boundary layer processes culminating in leading edge vortex initiation were characterized in detail across a broad α^+ and Re_c range. α^+ extended from elevated levels, down through quasi-steady and into the steady regime. Re_c values were in the low and transitional range. Unsteady boundary layer events responded in consistent and orderly manner to parameter variations, and fluid dynamic mechanisms underlying these responses were postulated. The following specific conclusions can be stated.

The unsteady boundary layer evolves through four stages culminating in leading edge vortex emergence: 1) boundary layer reversal (shear stress minima accompanied by phase reversals); 2) incipient reattachment (rapid shear stress increases, phase reversals, and incipient standard deviation rises); 3) concluded reattachment (phase reversals and standard deviation maxima); and 4) leading edge vortex initiation and subsequent convection (shear stress maxima).

As α^+ increases, constant viscous timescales coupled with faster pitching postpone boundary layer reversal and reattachment to higher α. Increasing α^+ also condenses vorticity production and enhances accumulation mechanisms, confining boundary layer reversal and reattachment to a region which is shorter as well as nearer the airfoil leading edge.

At sufficiently high α^+ boundary layer reversal and reattachment take place simultaneously at multiple surface locations. Whether these events occur at single or multiple locations, reversal and reattachment sites maintain a one-to-one correspondence, pointing to a topological consistency and causal relationships.

Quasi-steady boundary layer reversal movement and static boundary layer separation progress in analogous fashion, but quasi-steady and static reattachment differ significantly. Although unsteadiness does fundamentally change the flow physics of separation, it profoundly alters the fluid dynamics governing reattachment. The precise mechanism for unsteady reattachment remains uncertain, likely being mediated by interactions different from those governing steady reattachment.

Consistent with enhanced vorticity concentrations caused by boundary layer and shear layer thinning, higher Re_c prompts unsteady boundary layer reversal and reattachment to occur sooner at lower α. However, changes in reversal and reattachment elicited by Re_c variations are much less pronounced than those driven by α^+.

These investigations have characterized unsteady boundary layer processes that initiate and shape the development of unsteady vortex dominated flows on pitching lifting surfaces. This knowledge, in conjunction with similar information from other sources, provides information useful for developing modeling strategies and control methodologies applicable to the early stages of unsteady vortex formation. This, in turn, will provide a basis for alleviating the adverse effects of unsteady vortex dominated flows in wind energy machines, rotorcraft, and maneuvering fixed wing aircraft.

References

[1]Carr, L. W., "Progress in Analysis and Prediction of Dynamic Stall," *Journal of Aircraft*, Vol. 25, No. 1, 1988, pp. 6–17.

[2]Carr, L. W. (ed.), "Physics of Forced Unsteady Boundary Layer Reversal," NASA CP 3144, March 1992.

[3]Carr, L., McAlister, K., and McCroskey, W., "Analysis of the Development of Dynamic Stall Based on Oscillating Airfoil Experiments," NASA TN D-8382, Jan. 1977.

[4]Koromilas, C., and Telionis, D., "Unsteady Laminar Separation: An Experimental Study," *Journal of Fluid Mechanics*, Vol. 97, Pt. 2, 1980, pp. 347–384.

[5]Schreck, S., and Luttges, M., "Occurrence and Characteristics of Flow Reversal During the Genesis of Unsteady Separated Flows," AIAA Paper 89-0142, Jan. 1989.

[6]Schreck, S., and Faller, W., "Pitch Rate and Reynolds Number Effects on Unsteady Boundary Layer Transition and Separation," *Journal of Aircraft*, Vol. 35, No. 1, 1998, pp.46–52.

[7]Schreck, S., Faller, W., and Helin, H., "Pitch Rate and Reynolds Number Effects on Unsteady Boundary-Layer Transition and Separation," *Journal of Aircraft*, Vol. 35, No. 1, 1998, pp. 46–52.

[8]Kiedaisch, J., and Acharya, M., "Investigation of Incipient Dynamic Stall over Pitching Airfoils Using Hot-Film Sensors," AIAA Paper 97-0656, Jan. 1997.

[9]Kiedaisch, J., and Acharya, M., "Investigation of Unsteady Separation over Pitching Airfoils at High Reynolds Numbers," AIAA Paper 98-2975, June 1998.

[10]Lee, T., and Basu, S., "Measurement of Unsteady Boundary Layer Developed on an Oscillating Airfoil Using Multiple Hot-Film Sensors," *Experiments in Fluids*, Vol. 25, No. 2, 1998, pp. 108–117.

[11]Visbal, M. R., "On the Formation and Control of the Dynamic Stall Vortex on a Pitching Airfoil," AIAA Paper 91-0006, Jan. 1991.

[12]Gendrich, C., Koochesfahani, M., and Visbal, M., "Effects of Initial Acceleration on the Flow Field Development Around Rapidly Pitching Airfoils," *Journal of Fluids Engineering*, Vol. 117, No. 1, 1995, pp. 45–49.

[13]Ghia, K., Yang, J., Osswald, G., and Ghia, U., "Study of the Role of Unsteady Boundary Layer Reversal in the Formation of Dynamic Stall Vortex," AIAA Paper 92-0196, Jan. 1992.

[14]Knight, D., and Choudhuri, P., "2-D Unsteady Leading Edge Boundary Layer Reversal on a Pitching Airfoil," AIAA Paper 93-2977, July 1993.

[15]Reisenthel, P., "Further Results on the Reynolds Number Scaling of Incipient Leading Edge Stall," AIAA Paper 95-0780, Jan. 1995.

[16]Ericsson, L., "What About Transition Effects?," AIAA Paper 88-0564, Jan. 1988.

[17]Lorber, P., and Carta, F., "Unsteady Transition Measurements on a Pitching Three-Dimensional Wing," *Proceedings of the 5th Symposium on Numerical and Physical Aspects of Aerodynamic Flows*, edited by T. Cebici, California State Univ., Long Beach, CA, Jan. 1992.

[18]Wilder, M., Chandrasekhara, M., and Carr, L., "Transition Effects on Compressible Dynamic Stall of Transiently Pitching Airfoils," AIAA Paper 93-2978, July 1993.

[19]Carr, L., and Cebeci, T., "Boundary Layers on Oscillating Airfoils," *Proceedings of the 3rd Symposium on Numerical and Physical Aspects of Aerodynamic Flows*, edited by T. Cebici, California State Univ., Long Beach, CA, Jan. 1985.

[20]Stack, J., Mangalam, S., and Kalburgi, V., "The Phase Reversal Phenomenon at Flow Separation and Reattachment," AIAA Paper 88-0408, Jan. 1988.

[21]Mangalam, S., Stack, J., and Sewall, W., "Simultaneous Detection of Separation and Transition in Surface Shear Layers," Cesme, Turkey, AGARD-CP-438, Oct. 1988.

[22]Robinson, M., Walker, J., and Wissler, J., "Unsteady Surface Pressure Measurements on a Pitching Rectangular Wing," *Unsteady Separated Flow Workshop II Proceedings*, USAFA, 1988, pp. 225–237.

[23]Schreck, S., Addington, G., and Luttges, M., "Flow Field Structure and Development near the Root of a Straight Wing Pitching at Constant Rate," AIAA Paper 91-1793, June 1991.

[24]O'Meara, M., and Mueller, T., "Laminar Separation Bubble Characteristics on an Airfoil at Low Reynolds Numbers," *AIAA Journal*, Vol. 25, No. 8, 1987, pp. 1033–1041.

[25]Luttges, M., and Kennedy, D., "Initiation and Use of Three-Dimensional Unsteady Separated Flows," *Unsteady Separated Flow Workshop II Proceedings*, 1988, pp. 211–222.

[26]Cherry, N., Hillier, R., and Latour, M., "Unsteady Measurements in a Separated and Reattaching Flow," *Journal of Fluid Mechanics*, Vol. 144, 1984, pp. 13–46.

[27]Acharya, M., and Metwally, M., "Evolution of the Unsteady Pressure Field and Vorticity Production at the Surface of a Pitching Airfoil," AIAA Paper 90-1472, June 1990.